Inorganic Chemistry
ARTICLE
pubs.acs.org/IC

Layered Perovskite-Like $Pb_2Fe_2O_5$ Structure as a Parent Matrix for the Nucleation and Growth of Crystallographic Shear Planes

Dmitry Batuk,[†] Joke Hadermann,[†] Artem Abakumov,*[,†] Thomas Vranken,[‡] An Hardy,[‡,§] Marlies Van Bael,[‡,§] and Gustaaf Van Tendeloo[†]

[†]EMAT, University of Antwerp, Groenenborgerlaan 171, 2020 Antwerp, Belgium

[‡]Institute for Materials Research, Inorganic and Physical Chemistry, Hasselt University, Agoralaan Building D, 3590 Diepenbeek, Belgium

[§]Division IMOMEC, IMEC, Agoralaan Building D, 3590 Diepenbeek, Belgium

Supporting Information

ABSTRACT: The $Pb_2Fe_2O_5$ compound with a layered intergrowth structure has been prepared by a solid-state reaction at 700 °C. The incommensurate compound crystallizes in a tetragonal system with $a = 3.9037(2)$ Å, $c = 3.9996(4)$ Å, and $\mathbf{q} = 0.1186(4)\mathbf{c}^*$, or when treated as a commensurate approximant, $a = 3.9047(2)$ Å, $c = 36.000(3)$ Å, space group $I4/mmm$. The crystal structure of $Pb_2Fe_2O_5$ was resolved from transmission electron microscopy data. Atomic coordinates and occupancies of the cation positions were estimated from high-angle annular dark-field scanning transmission electron microscopy data. Direct visualization of the positions of the oxygen atoms was possible using annular bright-field scanning transmission electron microscopy. The structure can be represented as an intergrowth of perovskite blocks and partially disordered blocks with a structure similar to that of the Bi_2O_2 blocks in Aurivillius-type phases. The A-cation positions at the border of the perovskite block and the cation positions in the Aurivillius-type blocks are jointly occupied by Pb^{2+} and Fe^{3+} cations, resulting in a layer sequence along the c axis: $-PbO-FeO_2-PbO-FeO_2-Pb_{7/8}Fe_{1/8}-O_{1-x}-Fe_{5/8}Pb_{3/8}-O_2-Fe_{5/8}Pb_{3/8}-$. Upon heating, the layered $Pb_2Fe_2O_5$ structure transforms into an anion-deficient perovskite modulated by periodically spaced crystallographic shear (CS) planes. Considering the layered $Pb_2Fe_2O_5$ structure as a parent matrix for the nucleation and growth of CS planes allows an explanation of the specific microstructure observed for the CS structures in the Pb−Fe−O system.

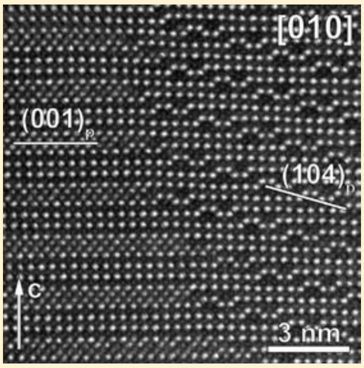

1. INTRODUCTION

In many oxide systems, the oxygen nonstoichiometry can result in a set of intermediate phases with well-defined compositions. Such crystallographically and compositionally distinct phases can arise from the ordering of point vacancies.[1−3] A remarkable example among perovskite-type structures is given by the Sr−Fe−O system. Increasing the concentration of oxygen vacancies in the cubic $SrFeO_3$ perovskite first leads to the $Sr_4Fe_4O_{11}$ and $Sr_8Fe_8O_{23}$ compounds with ordered FeO_5 pyramids and FeO_6 octahedra,[4] then to the $Sr_2Fe_2O_5$ brownmillerite with alternating layers of FeO_4 tetrahedra and FeO_6 octahedra,[5,6] and finally to $SrFeO_2$ with the so-called "infinite layer"-type structure consisting of layers of corner-sharing FeO_4 squares with the strontium cations in between.[7] However, if A cations with a lone electron pair (Pb^{2+} and Bi^{3+}) are added to the anion-deficient perovskite structure, another scenario can be realized, where oxygen vacancies are eliminated by periodically spaced translational interfaces.[8,9] The crystallographic properties of such interfaces recall those of the crystallographic shear (CS) planes, which account for oxygen nonstoichiometry in the oxides with ReO_3- or rutile-based structures. Along the CS plane, one part of the basic structure is displaced with respect to another by a vector that is a fraction of the translation of the basic lattice. This displacement eliminates point vacancies by changing the connectivity of the metal−oxygen polyhedra along the CS plane (for example, from corner-sharing to edge-sharing).[10,11] Such a mechanism, common in many binary or mixed oxides with the ReO_3-type structure, was thought not possible for perovskites, being prevented by the A cations in the cuboctahedral cavities of the ReO_3-type framework. However, since the presence of CS planes in anion-deficient perovskites was demonstrated,[8,9] this family of compounds has been expanded and a rigorous description of these structures in terms of (3 + 1)-dimensional crystallography has been provided.[12−17]

However, many questions related to the anion-deficient perovskites with CS structures are still puzzling. One of the most intriguing materials is "$Pb_2Fe_2O_5$", which was shown to be a complex intergrowth of structures with different crystallographic orientations of the CS planes. Among them, the $Pb_{15}Fe_{16}O_{39}$ structure with the $1/2[110](104)_p$ CS planes dominates.[9] The material possesses a complex microstructure that involves

Received: January 31, 2011
Published: April 29, 2011

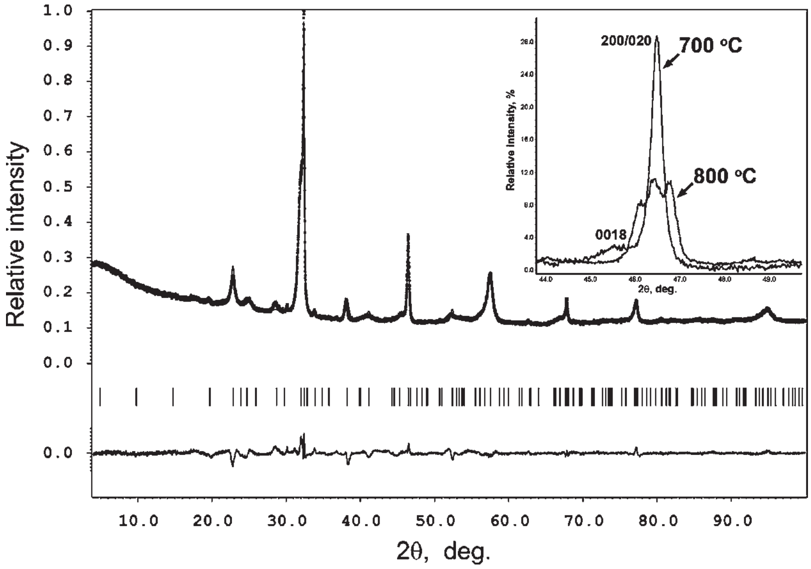

Figure 1. Experimental, calculated, and difference PXRD patterns of the sample prepared at 700 °C. Vertical bars mark the reflection positions of the *I*-centered tetragonal unit cell with $a = 3.9047(2)$ Å and $c = 36.000(3)$ Å. A comparison of the shapes of the $\{200\}_p$ perovskite subcell reflections for the samples annealed at 700 and 800 °C is shown in the inset.

numerous twinned microdomains and coherent intergrowths of structures with different $1/2[110](h0l)_p$ CS planes.[18] The formation mechanism of the CS structures with such a rich defect microstructure is still unclear. At least, the formation mechanisms proposed for the CS structures in binary ReO_3-type oxides are not directly applicable here. The mechanisms based on a cooperative cation migration, dislocation-limited anion vacancy loop, or "hairpin" growth all imply the existence of a preformed parent structure, such as WO_3 in the case of the W_nO_{3n-2} CS structures.[19−22] However, an existence of the $PbFeO_3$ perovskite is not reported, and it cannot serve as the parent structure for CS planes in the Pb−Fe−O system.

In this contribution, we demonstrate that not a simple perovskite but a more complex partially disordered layered intergrowth structure with the $Pb_2Fe_2O_5$ composition is first formed in the Pb−Fe−O system and then serves as a parent structure for the nucleation and growth of CS planes. The symmetry and chemical composition of this parent phase satisfactorily explain the main microstructural features observed in the "$Pb_2Fe_2O_5$" material. The crystal structure of the layered $Pb_2Fe_2O_5$ was completely resolved from transmission electron microscopy data, including atomic coordinates, occupancies of the cation positions, and direct visualization of the positions of the oxygen atoms.

2. EXPERIMENTAL SECTION

Samples were prepared by a solid-state synthesis as well as by the sol−gel method. The solid-state synthesis was conducted from metal oxides PbO and Fe_2O_3 (Aldrich, 99.9% pure). The initial materials were mixed with a metal ratio of Pb:Fe = 7:8 and rigorously ground. The powder was pressed into pellets and annealed at 700−800 °C for up to 500 h, with intermediate regrinding each 50 h.

The compositions with the Pb:Fe ratios of 7:8, 9:10, 15:16, and 1:1 were prepared by sol−gel synthesis starting from aqueous solutions of iron (0.7 mol·L^{-1}) and lead (0.7 mol·L^{-1}) citrates. They were prepared from commercial citrates as reported earlier.[23,24] These monometal ion precursor solutions were mixed in appropriate volumes to obtain a multimetal ion solution with a required molar ratio and a concentration of 0.3 mol·L^{-1}. In order to obtain a stable and gellable solution, supplemental citric acid (1.5 mol·L^{-1}, $C_6H_8O_7$, 99%, Aldrich) was added to reach a total citric acid to metal ratio of 2:1. The pH was increased to 8.0 by the dropwise addition of ammonia (NH_3, 32%, Merck, extra pure). The solution was evaporated in a laboratory furnace at 60 °C from a Petri dish, which yielded a clear precursor gel. This gel was heated in an air-flushed (0.5 L·min^{-1}) tube furnace at a heating rate of 5 °C·min^{-1}, followed by an isothermal period of 2 h at 600−700 °C, after which the sample was furnace-cooled to room temperature.

The powder X-ray diffraction (PXRD) patterns were recorded on a Huber G670 Guinier diffractometer (Cu Kα_1 radiation, curved Ge(111) monochromator, transmission mode, image plate).

The samples for transmission electron microscopy (TEM) investigation were made by crushing the powder in methanol and depositing the suspension on a copper grid covered with a holey carbon film. Selected-area electron diffraction (ED) and high-angle annular dark-field scanning transmission electron microscopy (HAADF-STEM) images were taken on a FEI Tecnai G2 microscope operated at 200 kV. Part of the HAADF-STEM images and annular bright-field scanning transmission electron microscopy (ABF-STEM) data were obtained on a FEI Titan 50-80 microscope operated at 300 kV and equipped with a probe aberration corrector. The STEM image simulations were performed using the *QSTEM 2.0* software.[25]

Iodometric titration was employed to determine the oxidation state of iron in the compound. The sample was rigorously ground with acetone and dried. An exact amount (~0.15 g) of a very fine powder was leached with 45 mL of a solution bearing 6.7% KI and 3.3 M HCl. Dissolution of the material was accompanied by an intense I_2 release and the formation of lead iodide. The suspension was leached for 24 h in the dark. Then, the volume was adjusted to 50 mL with water, and three aliquots of 15 mL were titrated with the $Na_2S_2O_3$ solution. Although PbI_2 is a relatively poorly soluble compound, it does not affect iron dissolution, which was confirmed by PXRD and energy-dispersive X-ray (EDX) analysis. The solid residue after leaching consists of PbI_2 only. In order to avoid any side effects, a reference experiment was performed. An aliquot of the standardized $K_2Cr_2O_7$ solution bearing approximately the same amount of oxidant as the sample under investigation, was treated in the same way. Thus, the amount of iodine formed due to side processes was determined and taken into account within the calculations.

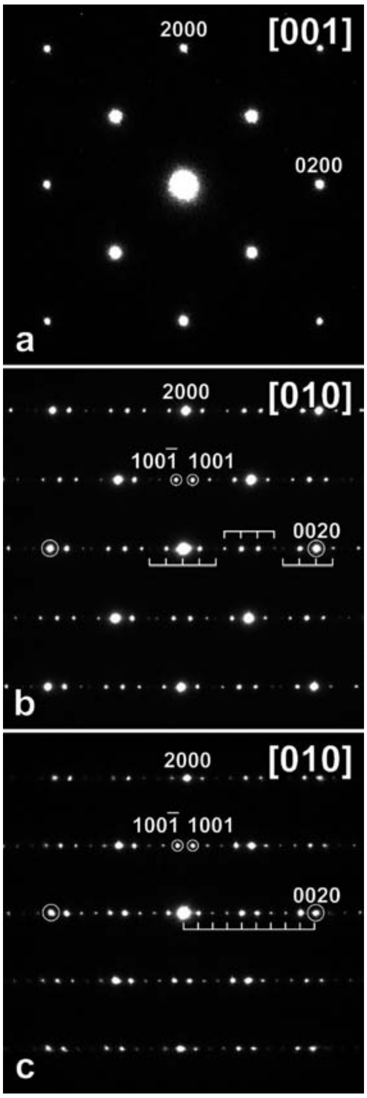

Figure 2. ED patterns of the perovskite-based phase in the samples prepared at 700 °C. The patterns are indexed in a tetragonal unit cell with $a \approx c \approx 3.9$ Å and the modulation vector $\mathbf{q} = \gamma \mathbf{c}^*$ (a, the [001] zone; b, the [010] zone for $\gamma = {}^1/_8$; c, the [010] zone for $\gamma = {}^1/_9$; the step of the brackets corresponds to 2**q**).

3. RESULTS

3.1. Crystal Structure of $Pb_2Fe_2O_5$. When the solid-state reaction was carried out at 600 °C, no formation of the perovskite-based phases was observed and the samples consisted of a mixture of PbO and $PbFe_{12}O_{19}$. Independent from the initial cation ratio and the synthesis technique (solid-state reaction of oxides or decomposition of the sol−gel precursor), all samples annealed at 700 °C demonstrate very similar PXRD patterns (a representative one is shown in Figure 1). The positions of the strongest peaks on this pattern roughly correspond to a cubic perovskite structure with $a \approx 3.9$ Å. The reflections demonstrate a very strong asymmetry and anisotropic broadening, which reflects a distortion of the parent perovskite structure and/or the presence of numerous defects. These features do not allow reliable ab initio indexation of the PXRD patterns.

ED patterns of this perovskite-based material are shown in Figure 2. Two kinds of ED patterns taken along the perovskite cubic directions were observed. The ED pattern in Figure 2a can be indexed on a tetragonal lattice with $a \approx 3.9$ Å; the reflections with an odd sum of the Miller indexes are systematically absent on this pattern. The ED patterns in Figure 2b,c demonstrate rows of superlattice reflections along the $[001]_p$ direction. The positions of the superlattice reflections can be described with a modulation vector $\mathbf{q} = \gamma \mathbf{c}^*$. The γ value varies for different crystallites, being, however, always between $\gamma = {}^1/_8$ (Figure 2b) and ${}^1/_9$ (Figure 2c). All ED patterns can be consistently indexed using a tetragonal unit cell with $a = b \approx c \approx 3.9$ Å and a modulation vector $\mathbf{q} = \gamma \mathbf{c}^*$, where $\gamma = {}^1/_8 - {}^1/_9$. The observed reflection condition $h + k + l + m = 2n$ suggests the $[{}^1/_2, {}^1/_2, {}^1/_2, {}^1/_2]$ centering vector.

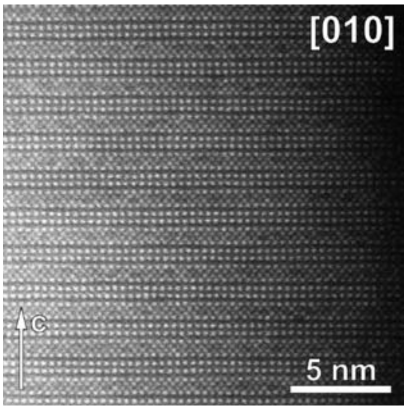

Figure 3. [010] HAADF-STEM image of the $\gamma = {}^1/_9$ structure.

The HAADF-STEM image of the $\gamma = {}^1/_9$ structure (Figure 3) reveals that the modulation is caused by the stacking of quasi-two-dimensional structure blocks, forming a long-range-ordered periodic array. The detailed structure of the constituent blocks can be understood from a combination of the HAADF-STEM and ABF-STEM images (Figures 4 and 5). On HAADF-STEM images, the brightness of a spot related to an atomic column scales as Z^n $(1 < n < 2)$, where Z is the atomic number of the projected column. The crystal structure will be further discussed in the frame of the body-centered tetragonal supercell with lattice parameters $a \approx a_p \approx 3.9$ Å and $c \approx 9c_p \approx 36$ Å. The [001] HAADF-STEM image reveals a square mesh of dots of identical brightness with a periodicity of $\sqrt{2}a_p$, in agreement with the proposed tetragonal symmetry (Figure 4a). Along this viewing axis, the cationic columns of different blocks are projected onto each other, being shifted by the centering translation. The [010] HAADF-STEM image provides more information on the internal structure of the blocks (Figure 4b). A visual inspection of the image reveals three types of dots with different brightness. The brighter dots form a square mesh with a periodicity of a_p; each square is centered with a weak dot. This image is typical for the perovskite structure, where the A positions are occupied by heavy lead cations ($Z = 82$) and the B positions are taken by the iron cations ($Z = 26$). Thus, the brightest and weakest dots correspond to the projections of the lead and FeO columns, respectively. The perovskite blocks have a thickness of $3a_p$ along the c axis and are centered at the $z = 0$ and ${}^1/_2$ planes of the tetragonal unit cell. Between the perovskite blocks, there are layers of dots forming a chess-board pattern; the brightness of these dots reveals that they correspond to atomic columns with a mixture of lead and iron. In fact, the quantitative measurement of the

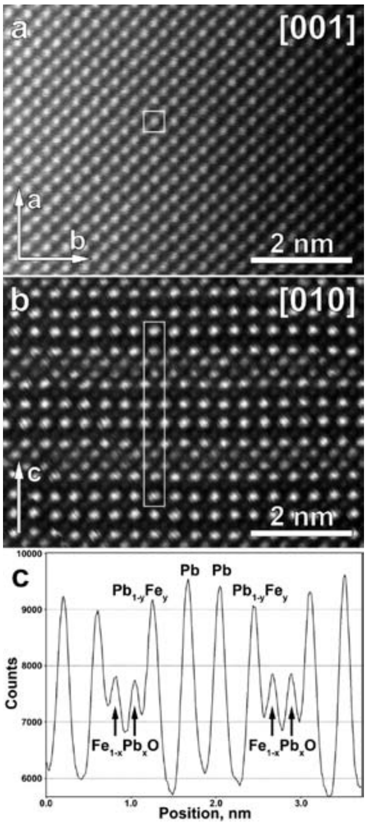

Figure 4. HAADF-STEM images of the $\gamma = {}^1/_9$ structure along the [001] (a) and [010] (b) zone axes. The tetragonal a_p, b_p, and $9c_p$ supercell is marked with rectangles. The plot c is the intensity profile measured over one period of the supercell along the c axis, marked with a white rectangle in part b. This shows the intensity averaged in the $a-b$ plane and reveals the z coordinate and the occupancy factor of the atomic columns.

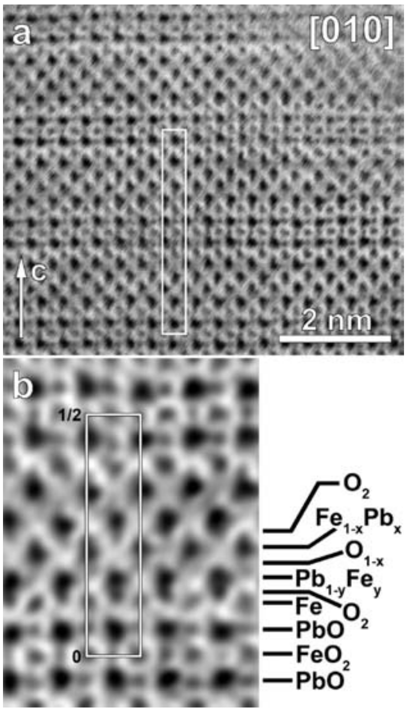

Figure 5. Experimental [010] ABF-STEM image (a) and the enlarged part of the image after low-pass filtering (b). The tetragonal supercell is marked with a rectangle on image a, whereas half of the cell is indicated on image b.

intensity of the dots by averaging over at least 20 unit cells indicates that the outer A-cation columns of the perovskite blocks demonstrate a slightly lower brightness than the two A-cation columns inside the perovskite blocks (see the intensity plot in Figure 4c). This suggests a cation arrangement for the projected atomic columns on the [010] HAADF-STEM image as follows: Pb (two layers of bright dots inside the perovskite blocks), $Pb_{1-y}Fe_y$ (outer layers of bright dots of the perovskite block), $Fe_{1-x}Pb_x$ (dots of intermediate brightness forming a chess-board pattern separating the perovskite blocks), and Fe (weak dots of the perovskite block).

Oxygen columns cannot be discerned on these HAADF-STEM images because of their low atomic number. The positions of the oxygen atoms were determined using a [010] ABF-STEM image (Figure 5). In contrast to the HAADF-STEM imaging, where the annular detector registers mainly the electrons inelastically scattered by the sample, the annular detector in the ABF-STEM imaging mode spans an angular range within the illumination cone of the focused electron probe, picking up the signal consisting of elastic and thermal diffuse scattering contributions.[26,27] The ABF-STEM images demonstrate an “absorptive” type of contrast, where the regions of higher atomic potential look darker on a bright background. It was demonstrated that, because of the impact of the elastic scattering, columns of light elements can be observed together with the heavy atomic columns on ABF-STEM images, in contrast to HAADF-STEM images.[26,27] The ABF-STEM images are quite robust toward sample thickness variation. The darkness of the spots from atomic columns scales approximately as $Z^{1/3}$, at least for atoms with large Z. The signal from the light atomic columns slightly depends on the sample thickness, vanishing with an increase in the sample thickness, but this dependence is not crucial and does affect the interpretation of the image.[27] Thus, a qualitative straightforward interpretation of the ABF-STEM images is possible, especially when the complementary HAADF-STEM image is available to ensure assignment of atomic entities to the atomic column dots.

Figure 5 shows an unfiltered experimental [010] ABF-STEM image and its enlarged part after application of a low-pass filter, cutting out spatial frequencies above the information limit of the microscope. The sequence of the atomic layers along the c axis can be directly retrieved from these images. The perovskite (FeO_2) layer is positioned at $z = 0$, being sandwiched between two PbO layers. The next FeO_2 perovskite layer is not flat and appears to be split: the iron and oxygen atoms in this layer have different z coordinates. The outer $Pb_{1-y}Fe_y$ layers of the perovskite block do not contain separate columns of oxygen atoms. The oxygen atoms are absent as well in the $Fe_{1-x}Pb_x$ layers, but the O_2 layer is present between these layers. It should be noted that faint dots, possibly indicating oxygen columns, are irregularly present between the $Pb_{1-y}Fe_y$ and $Fe_{1-x}Pb_x$ layers. This can be interpreted as a layer of partially occupied oxygen positions (O_{1-x}).

The occupancy factors for $Pb_{1-y}Fe_y$ and $Fe_{1-x}Pb_x$ can be estimated from the brightness of the corresponding spots on the HAADF-STEM image (Figure 4b). The intensities of the dots corresponding to the FeO and Pb columns of the perovskite blocks were used for calibration of the intensities assuming an $I = aZ^n + b$ dependence, where Z is the sum of the atomic numbers of the elements along the column and b is the constant background contribution. The n value is usually between 1 and 2, but because only two experimental points were available for calibration, we assumed the linear $I(Z)$ dependence. Because of the short projected distance between the $Fe_{1-x}Pb_x$ and oxygen atoms from the neighboring (O_2) layer (~1.1 Å), the $Fe_{1-x}Pb_xO$ columns were considered. The $y \approx {}^1/_8$ and $x \approx {}^3/_8$ values were derived from the estimated Z values. Thus, the layer sequence along the c axis can be written as

$$– (PbO) – (FeO_2) – (PbO) – (FeO_2) – (Pb_{7/8}Fe_{1/8}) – (O_{1-x}) – (Fe_{5/8}Pb_{3/8}) – (O_2) – (Fe_{5/8}Pb_{3/8}) –$$

$$\vdash\!\!\text{————————}\ c/4\ \text{————————}\!\!\dashv$$

This results in the $Pb_9Fe_9O_{24-4x}$ chemical formula per unit cell. As deduced from the structure consideration below, the amount of oxygen atoms in the O_{1-x} layer should be equal to the amount of iron atoms in the $Fe_{5/8}Pb_{3/8}$ layers. This fixes the oxygen content according to the formula $Pb_9Fe_9O_{22.5}$ or $Pb_2Fe_2O_5$, which closely corresponds to the bulk composition of the samples and agrees with the results of the EDX analysis and the iodometric titration, demonstrating the oxidation state of iron to be 3.01(3)+. However, the $Pb_2Fe_2O_5$ composition should be considered as a tentative one. Most probably, this compound can have a homogeneity range because of a variable occupancy factor at the two cation positions and a variable oxygen content in the O_{1-x} layer. However, the evaluation of this homogeneity range is outside the possibilities of the techniques used in this work. One should also notice that the cation distribution in the $Fe_{5/8}Pb_{3/8}$ layers is not completely random. The intensity modulations along these layers are visible on the HAADF-STEM image (Figure 3). Although they are not periodic, they show short-range order in the iron and lead distribution within these layers.

For construction of the structure model, one can adopt the highest possible symmetry $I4/mmm$ compatible with the ED patterns. This symmetry fixes the x and y coordinates of the atoms in all layers to be either 0 or ${}^1/_2$. The z coordinates were estimated from the HAADF-STEM and ABF-STEM images. This was done by measuring the intensity profiles of the atomic rows along the z direction. The profiles were fitted with a set of Gaussian peaks in the *Fityk* software.[28] The parameters of the functions were used to determine relative atomic coordinates. However, it was demonstrated that, if atomic columns are projected too close to each other (such as the columns in the $Fe_{5/8}Pb_{3/8}$ and O_2 layers), their position on the ABF-STEM image may deviate from their real positions in the structure.[27] This makes applicability of the ABF-STEM image for a quantitative determination of the atomic positions questionable. In order to verify the proposed structure, the Rietveld refinement against PXRD data was performed. The refinement was performed within a commensurate approximation corresponding to the a_p, b_p, $9c_p$ tetragonal unit cell [a = 3.9047(2) Å and c = 36.000(3) Å]. The anisotropic broadening was accounted for using a method described by Stephens.[29] The refined z coordinates of the cations were found to be very close to those derived from the TEM data. However, a reliable refinement of the atomic coordinates of the oxygen atoms was not achieved because of the poor quality of the PXRD data, which deteriorated because of the high concentration of defects and deviations from the commensurate unit cell used in the refinement. Indeed, a close inspection of the experimental and calculated PXRD profiles demonstrates deviations in the positions of the reflections, which can be considered as satellites with respect to the $a_p \times a_p \times a_p$ basic structure. A more precise fit of the PXRD profile can be achieved in an incommensurate approximation with a = 3.9037(2) Å, c = 3.9996(4) Å, and $\mathbf{q} = 0.1186(4)\mathbf{c}^*$, with an average γ value between ${}^1/_8$ and ${}^1/_9$, in agreement with the ED data. Nevertheless, the Rietveld refinement in a commensurate approximation with the atomic coordinates of the oxygen atoms as determined from TEM data results in relatively low reliability factors (R_I = 0.052, R_P = 0.023, and R_{wP} = 0.033). This reflects that the structure model correctly reproduces the major structural features of $Pb_2Fe_2O_5$. The experimental, calculated, and difference PXRD patterns are shown in Figure 1. The atomic coordinates as derived from the TEM data and refined from PXRD data are provided in Table S1 of the Supporting Information. Using these atomic coordinates and occupancy factors, the theoretical HAADF-STEM and ABF-STEM images were calculated. Both simulated images demonstrate a remarkably good agreement with the experimental ones (Figure 6).

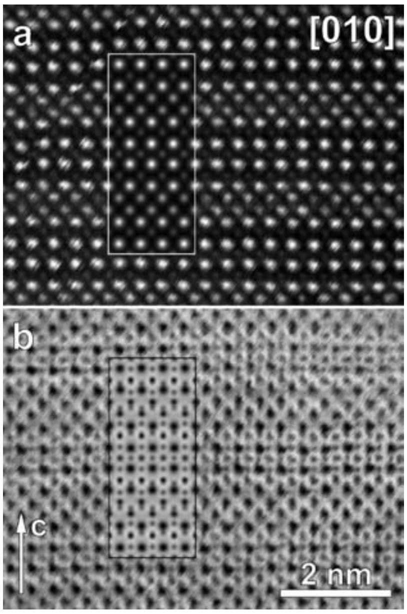

Figure 6. Simulated HAADF-STEM and ABF-STEM images, shown against the experimental ones.

The $Pb_2Fe_2O_5$ structure is shown in Figure 7. For structure consideration, the cation positions in the mixed layers will be assumed to be occupied by the prevailing type of cation (i.e., lead in the $Pb_{7/8}Fe_{1/8}$ layer and iron in the $Fe_{5/8}Pb_{3/8}$ layer). The iron atoms at the FeO_2 layers at the center of the perovskite block are in octahedral coordination, but the iron atoms at the periphery of the perovskite block (the split layer marked as Fe and O_2) adopt a coordination closer to that of a square pyramid because of the shift of the O_2 layer toward the $Pb_{1-y}Fe_y$ layer. The coordination environment of these iron atoms is completed by the oxygen atoms from the partially occupied O_{1-x} layer, but this Fe–O distance is obviously longer so that coordination can be described as 5 + 1. The two $Fe_{1-x}Pb_x$ layers, together with the O_2 layer between them, form a fragment of the fluorite-type structure compressed along the c axis: the cations form a distorted

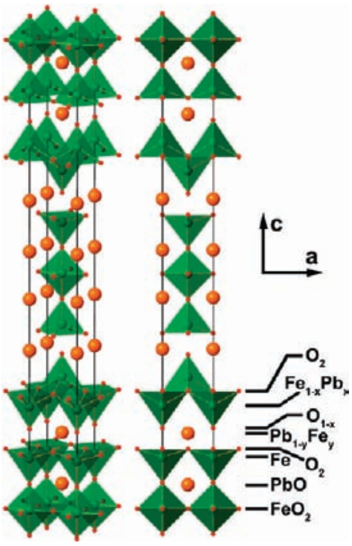

Figure 7. Model for the tetragonal $Pb_2Fe_2O_5$ intergrowth structure. Iron atoms are inside of the octahedra and tetragonal pyramids. Lead and oxygen atoms are shown as large orange and small red spheres, respectively.

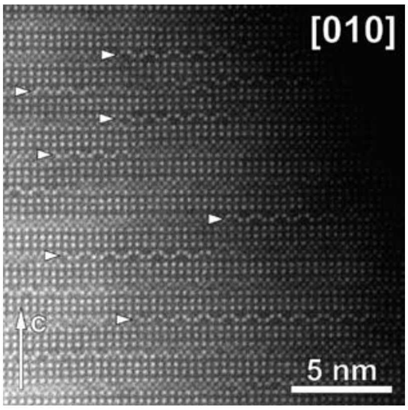

Figure 8. [010] HAADF-STEM image showing fragments of the composite $1 \times {}^{1}/_{2}[110](101)_p + 1 \times {}^{1}/_{2}[110](\bar{1}01)_p$ (marked with arrowheads) interfaces in the matrix of the tetragonal $Pb_2Fe_2O_5$ structure.

close-packed motif, and the oxygen atoms are situated at the tetrahedral interstices. This strongly resembles the Bi_2O_2 blocks in Aurivillius-type intergrowth structures. The oxygen atoms of the O_2 layers form the square base of the tetragonal pyramidal coordination of the iron atoms from the $Fe_{1-x}Pb_x$ layers. The apical vertex of the pyramid is formed by the oxygen atoms of the O_{1-x} layer. By sharing their equatorial edges, the pyramids form a layer with their apical vertexes pointing up and down in a chessboard manner. Because the oxygen atoms of the O_{1-x} layer are directly linked to the iron atoms in the $Fe_{1-x}Pb_x$ layer, it is logical to expect the same occupancy factors for these positions. If the position in the $Fe_{1-x}Pb_x$ layer is taken in by lead, the apical oxygen atom in the O_{1-x} layer is absent, resulting in an asymmetric 4-fold coordination typical for the Pb^{2+} cations. The lead atoms in the $Pb_{1-y}Fe_y$ layer also have an asymmetric 4-fold coordination, which is probably completed by the lone electron pair. A minor amount of Fe^{3+} cations (12.5%) is found in this position. Such asymmetric 4-fold coordination is not characteristic for the Fe^{3+} cations, and one can expect local oxygen rearrangement, which would lead to CN = 5 for these cations. However, because of the small amount of the iron cations in this position, the details of this local oxygen environment are difficult to unravel from the TEM data.

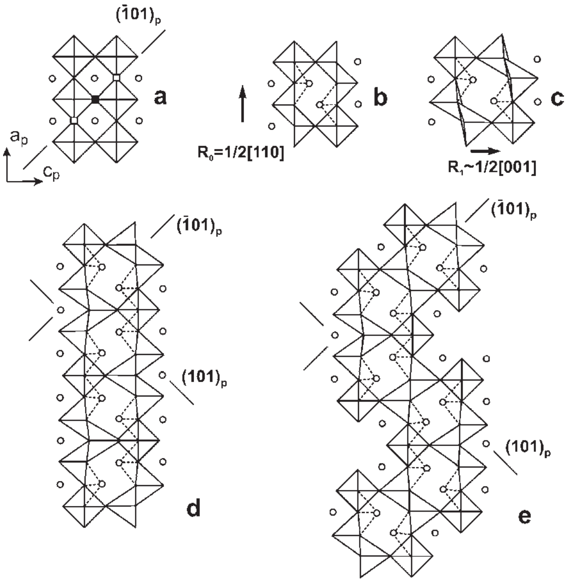

Figure 9. Construction of the composite interfaces. The basic perovskite structure with oxygen vacancies at the $(\bar{1}01)_p$ plane (a), application of the shear operation (b), application of relaxation shift (c), joining of the $(101)_p$ and $(\bar{1}01)_p$ parts into the composite $1 \times {}^{1}/_{2}[110](101)_p + 1 \times {}^{1}/_{2}[110](\bar{1}01)_p$ interface (d), and the composite $2 \times {}^{1}/_{2}[110](101)_p + 2 \times {}^{1}/_{2}[110](\bar{1}01)_p$ interface (e).

3.2. $Pb_2Fe_2O_5$ as a Parent Matrix for CS Planes. The tetragonal $Pb_2Fe_2O_5$ structure observed in the samples prepared at 700 °C is destroyed by heating the material at 800 °C. This can be clearly seen from a comparison of the shapes of the $\{200\}_p$ perovskite subcell reflections (see the inset in Figure 1). For the 700 °C sample, there is a sharp peak corresponding to the 200/020 reflections of the tetragonal structure. After annealing at 800 °C, the $\{200\}_p$ perovskite reflection splits into three reflections because of a monoclinic distortion of the perovskite subcell. This distortion is introduced by the periodic arrangement of the translational interfaces (CS planes) in the perovskite structure, as was demonstrated before for the $Pb_2Fe_2O_5$ sample prepared at 800 °C.[9] The transformation of the tetragonal $Pb_2Fe_2O_5$ structure into arrays of CS planes can be monitored by investigating the defect structure of the sample prepared at 700 °C.

Figure 8 demonstrates a part of the tetragonal $Pb_2Fe_2O_5$ structure, where Aurivillius-type blocks interleave in the *ab* plane with blocks of apparently a different cationic arrangement. This is clearly visible as segments in which the lead columns are arranged in a wavy manner. The known building principles of CS structures in perovskites allow us to propose an atomic model for such interfaces based on the positions of the cation columns observed on the HAADF-STEM image.[10,11]

The $Pb_2Fe_2O_5$ composition assumes an anion-deficient perovskite structure. Starting from a hypothetical parent perovskite with the anion vacancies in the $(\bar{1}01)_p$ plane (Figure 9a), one can introduce a shear operation, displacing one part of the perovskite

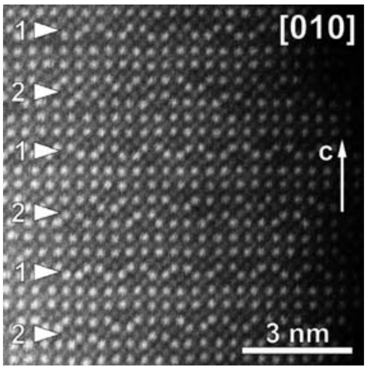

Figure 10. [010] HAADF-STEM image of quasi-periodic alternation of the 1 × $^1/_2$[110](101)$_p$ + 1 × $^1/_2$[110]($\bar{1}$01)$_p$ (marked as 1) and 2 × $^1/_2$[110](101)$_p$ + 2 × $^1/_2$[110]($\bar{1}$01)$_p$ (marked as 2) interfaces.

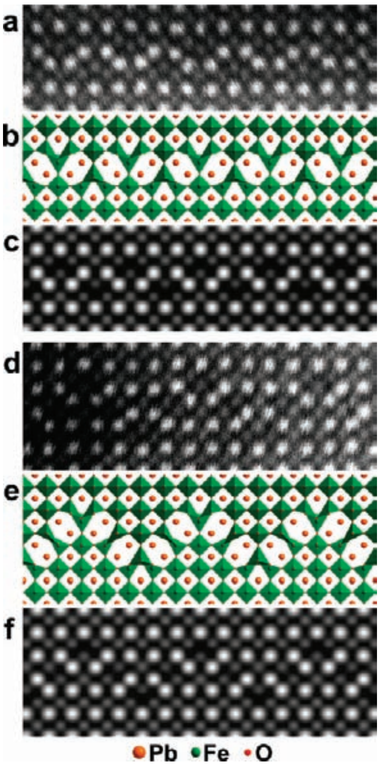

Figure 11. Experimental (a and d) [010] HAADF-STEM images of the 1 × $^1/_2$[110](101)$_p$ + 1 × $^1/_2$[110]($\bar{1}$01)$_p$ and 2 × $^1/_2$[110](101)$_p$ + 2 × $^1/_2$[110]($\bar{1}$01)$_p$ interfaces along with the corresponding structural models (b and e) and the simulated images (c and f).

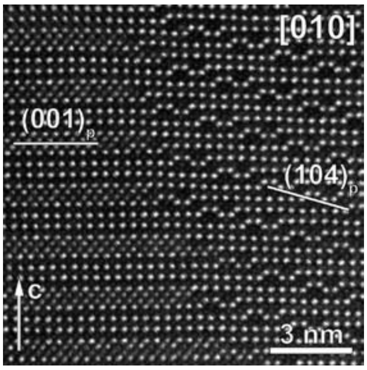

Figure 12. HAADF-STEM image of the coherent intergrowth between the tetragonal $Pb_2Fe_2O_5$ phase (left) and the $Pb_{15}Fe_{16}O_{39}$ phase with the $^1/_2$[110](104)$_p$ CS planes (right).

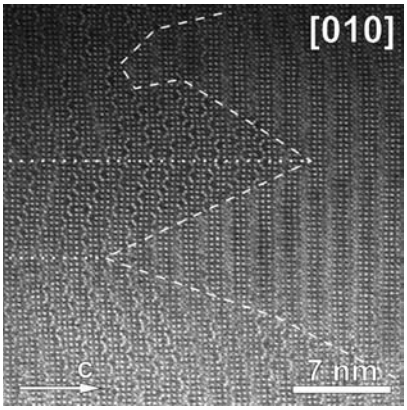

Figure 13. HAADF-STEM image showing the twinned domains of the $Pb_{15}Fe_{16}O_{39}$ phase growing at the expense of the tetragonal $Pb_2Fe_2O_5$ phase. The dashed line shows the $Pb_{15}Fe_{16}O_{39}$/tetragonal $Pb_2Fe_2O_5$ border, and the dotted line indicates the twin boundary within $Pb_{15}Fe_{16}O_{39}$.

structure with respect to another by the vector $^1/_2$[110]$_p$. This operation creates a plane consisting of fragments shown in Figure 9b. These fragments link together two perovskite blocks on both sides of the shear plane through the edge-sharing FeO_5 distorted tetragonal pyramids. The $^1/_2$[110]$_p$ displacement results in relatively short separations between the lead atoms in the two columns inside the six-sided tunnel formed by the FeO_5 pyramids and FeO_6 octahedra. An additional relaxation shift over ~$^1/_2$[001]$_p$ is necessary to restore reasonable Pb−Pb interatomic distances (Figure 9c). The interfaces between the perovskite blocks as shown in Figure 8 are confined to the (001)$_p$ plane and can be represented as alternating mutually perpendicular fragments of $^1/_2$[110](101)$_p$ and $^1/_2$[110]($\bar{1}$01)$_p$ CS planes (Figure 9d). Such composite $^1/_2$[110](001)$_p$ interfaces demonstrate a variable thickness due to an increase in the length of the constituting $^1/_2$[110](101)$_p$ and $^1/_2$[110]($\bar{1}$01)$_p$ fragments, as is shown in Figure 9c for an interface with double the length of the fragment. A HAADF-STEM image of an area with a quasi-periodic alternation of the 1 × $^1/_2$[110](101)$_p$ + 1 × $^1/_2$[110]($\bar{1}$01)$_p$ and 2 × $^1/_2$[110](101)$_p$ + 2 × $^1/_2$[110]($\bar{1}$01)$_p$ interfaces is shown in Figure 10. The proposed atomic structure of such interfaces is confirmed by the calculated HAADF-STEM images (Figure 11), showing an excellent agreement with the experimental images.

An interesting feature of the composite $^1/_2$[110](001)$_p$ interfaces is the complete ordering of the lead and iron cations. In contrast to the disordered Aurivillius-type blocks with mixed lead/iron columns, in the $^1/_2$[110](001)$_p$ interfaces, the lead and iron cations form separate columns and do not mix with each other. A complete ordering of these cations, at least at a local scale, would be expected in the structure obtained at nearly equilibrium conditions (i.e., at a temperature allowing efficient cation migration and at a time sufficient for cation rearrangement to be completed). Indeed, this occurs in "$Pb_2Fe_2O_5$" obtained at

800 °C, where no mixing of lead and iron on a local scale was observed (although numerous planar defects and intergrowths are present). One can speculate that the disordered metastable tetragonal $Pb_2Fe_2O_5$ structure obtained at 700 °C serves as a parent matrix for CS planes of different orientations, which grow in "$Pb_2Fe_2O_5$" at 800 °C, when the cation sublattice acquires sufficient mobility. This transformation is accompanied by a rearrangement of the lead and iron cations into separate columns. Observation of the ordered composite $^1/_2[110](001)_p$ interfaces in the sample annealed at 700 °C demonstrates that such a rearrangement already begins at this temperature and probably requires a much longer time to be completed because of kinetic limitations. An additional argument supporting this speculation is provided by the observation of numerous domains of the ordered CS planes intergrowing with the tetragonal $Pb_2Fe_2O_5$ structure. Figure 12 demonstrates such a coherent intergrowth of domains of the tetragonal $Pb_2Fe_2O_5$ structure and the $Pb_{15}Fe_{16}O_{39}$ structure with the $^1/_2[110](104)_p$ CS planes. A typical feature of the monoclinic $Pb_{15}Fe_{16}O_{39}$ structure is the presence of numerous microtwins with a mirror-reflected orientation of the $^1/_2[110](104)_p$ CS planes, occurring throughout the crystals.[17] The formation of such a heavily twinned structure can be due to the nucleation of twins from a preformed matrix with higher symmetry. The tetragonal $Pb_2Fe_2O_5$ structure possesses a set of mirror planes parallel to the *c* axis, which serve as twin planes upon transformation into the monoclinic $Pb_{15}Fe_{16}O_{39}$ structure. The growth of the multiply twinned structures from the tetragonal $Pb_2Fe_2O_5$ matrix is illustrated in Figure 13.

4. DISCUSSION

The structure of anion-deficient perovskite-based compounds in the Pb−Fe−O system drastically depends on the synthesis temperature. The solid-state reaction carried out at a temperature close to the melting point ($Pb_2Fe_2O_5$ melts incongruently at 870 °C[30]) results in a material with a complex intergrowth of anion-deficient perovskite structures modulated by CS planes. The $^1/_2[110](104)_p$ CS planes dominate, but the other orientations, such as $^1/_2[110](102)_p$ or $^1/_2[110](\bar{3}05)_p$, are also present. This reflects a remaining chemical inhomogeneity because the chemical composition and orientation of the CS planes are related to each other as $Pb_{4m+3n}Fe_{4(m+n)}O_{10m+9n}$, where *n* and *m* are the numbers of $\{101\}_p$ and $\{001\}_p$ parts constituting the $(h0l)_p$ CS plane. However, in spite of the large amount of intergrowths and planar defects, the lead and iron cations are ordered on a local scale, occupying positions with distinct oxygen coordination. Such an ordering is obviously not achieved at lower synthesis temperature, and a partially disordered layered perovskite compound is formed at 700 °C. In the structure of this compound, the perovskite blocks alternate with Aurivillius-type blocks, where the lead and iron cations jointly occupy common crystallographic positions. Although the $Pb_2Fe_2O_5$ composition of this material was estimated from the TEM data, the joint occupation of two crystallographic cation positions and one incompletely filled oxygen site implies that a homogeneity range is possible for this compound. If we assume the tetragonal disordered phase to be the parent matrix for the CS structures, $Pb_2Fe_2O_5$ should be the limiting point of the homogeneity range from the lead-rich side. Indeed, the general $Pb_{4m+3n}Fe_{4(m+n)}O_{10m+9n}$ formula of the CS structures in the Pb−Fe−O system assumes the Pb/Fe ratio to always be ≤ 1. The formula of the solid-state solutions is therefore expected to be $Pb_{2-\delta}Fe_{2+\delta}O_{5+\delta/2}$, where $\delta \geq 0$. The $Pb_{15}Fe_{16}O_{39}$ $^1/_2[110](104)_p$ CS structure dominates in the $Pb_2Fe_2O_5$ samples prepared at 800 °C, which requires a very small $\delta = 0.065$ value for the parent matrix. Apparently, a local variable chemical composition of the parent matrix accounts for the local observation of domains of CS structures with different orientations of the CS planes and different chemical compositions. Considering the tetragonal $Pb_2Fe_2O_5$ structure as the parent matrix also provides a satisfactory explanation for the multiple twin structure of the monoclinic CS phases. It should be noted that the formation of the CS structures not only requires cation ordering but also a rearrangement of the perovskite blocks. Regular steps should appear in the perovskite blocks, changing their orientation from $(001)_p$ in the parent tetragonal phase to $(h0l)_p$ in the final CS structure.

It is questionable whether the formation mechanism of the CS structures through the intermediate intergrowth structure with alternating perovskite and Aurivillius-type blocks can be applied to other chemical systems or whether it is unique for the Pb−Fe−O system. Our data on the structure and microstructure of the $(Pb,Bi)_{1-x}Fe_{1+x}O_{3-y}$ perovskites with $^1/_2[110](509)_p$ CS planes reflect that the latter seems to be the case.[18] $(Pb,Bi)_{1-x}Fe_{1+x}O_{3-y}$ demonstrates none of the microstructural features observed in the Pb−Fe−O system, which could be related to the presence of an intermediate phase with higher symmetry. One can speculate that adding Bi_2O_3 promotes cation diffusion and suppresses the formation of a metastable intermediate phase as observed in the Pb−Fe−O system.

■ ASSOCIATED CONTENT

Ⓢ Supporting Information. Crystallographic data in CIF format and a table with atomic coordinates for the $Pb_2Fe_2O_5$ structure model. This material is available free of charge via the Internet at http://pubs.acs.org.

■ AUTHOR INFORMATION

Corresponding Author

*E-mail: artem.abakumov@ua.ac.be. Phone: +32 3 265 32 59. Fax: +32 3 265 32 57.

■ ACKNOWLEDGMENT

The authors acknowledge financial support from the European Union under the Framework 6 program under a contract for an Integrated Infrastructure Initiative (Reference 026019 ESTEEM). D.B., J.H., T.V., A.H., and M.V.B. acknowledge financial support from the Research Foundation—Flanders (FWO G.0184.09N).

■ REFERENCES

(1) Anderson, M. T.; Vaughey, J. T.; Poeppelmeier, K. R. *Chem. Mater.* **1993**, *5*, 151–165.

(2) Stølen, S.; Bakken, E.; Mohn, C. E. *Phys. Chem. Chem. Phys.* **2006**, *8*, 429–447.

(3) Hadermann, J.; Van Tendeloo, G.; Abakumov, A. M. *Acta Crystallogr., Sect. A* **2005**, *61*, 77–92.

(4) Hodges, J. P.; Short, S.; Jorgensen, J. D.; Xiong, X.; Dabrowski, B.; Mini, S. M.; Kimball, C. W. *J. Solid State Chem.* **2000**, *151*, 190–209.

(5) Greaves, C.; Jacobson, A. J.; Tofield, B. C.; Fender, B. E. F. *Acta Crystallogr., Sect. B* **1975**, *31*, 641–646.

(6) D'Hondt, H.; Abakumov, A. M.; Hadermann, J.; Kalyuzhnaya, A. S.; Rozova, M. G.; Antipov, E. V.; Van Tendeloo, G. *Chem. Mater.* **2008**, *20*, 7188–7194.

(7) Tsujimoto, Y.; Tassel, C.; Hayashi, N.; Watanabe, T.; Kageyama, H.; Yoshimura, K.; Takano, M.; Ceretti, M.; Ritter, C.; Paulus, W. *Nature* **2007**, *450*, 1062–1065.

(8) Bougerol, C.; Gorius, M. F.; Grey, I. E. *J. Solid State Chem.* **2002**, *169*, 131–138.

(9) Abakumov, A. M.; Hadermann, J.; Bals, S.; Nikolaev, I. V.; Antipov, E. V.; Van Tendeloo, G. *Angew. Chem., Int. Ed.* **2006**, *45*, 6697–6700.

(10) Abakumov, A. M.; Hadermann, J.; Van Tendeloo, G.; Antipov, E. V. *J. Am. Ceram. Soc.* **2008**, *91*, 1807–1813.

(11) Antipov, E. V.; Abakumov, A. M.; Istomin, S. Ya. *Inorg. Chem.* **2008**, *47*, 8543–8552.

(12) Nikolaev, I. V.; D'Hondt, H.; Abakumov, A. M.; Hadermann, J.; Balagurov, A. M.; Bobrikov, I. A.; Sheptyakov, D. V.; Pomjakushin, V. Yu.; Pokholok, K. V.; Filimonov, D. S.; Van Tendeloo, G.; Antipov, E. V. *Phys. Rev. B* **2008**, *78*, 024426.

(13) Lepoittevin, C.; Hadermann, J.; Malo, S.; Perez, O.; Van Tendeloo, G.; Hervieu, M. *Inorg. Chem.* **2009**, *48*, 8257–8262.

(14) Malo, S.; Lepoittevin, C.; Perez, O.; Hebert, S.; Van Tendeloo, G.; Hervieu, M. *Chem. Mater.* **2010**, *22*, 1788–1797.

(15) Abakumov, A. M.; Hadermann, J.; Batuk, M.; D'Hondt, H.; Tyablikov, O. A.; Rozova, M. G.; Pokholok, K. V.; Filimonov, D. S.; Sheptyakov, D. V.; Tsirlin, A. A.; Niermann, D.; Hemberger, J.; Van Tendeloo, G.; Antipov, E. V. *Inorg. Chem.* **2010**, *49*, 9508–9516.

(16) Tzvetkov, P.; Petrova, N.; Kovacheva, D. *J. Alloys Compd.* **2009**, *485*, 862–866.

(17) Hadermann, J.; Abakumov, A. M.; Nikolaev, I. V.; Antipov, E. V.; Van Tendeloo, G. *Solid State Sci.* **2008**, *10*, 382–389.

(18) Abakumov, A. M.; Batuk, D.; Hadermann, J.; Rozova, M. G.; Sheptyakov, D. V.; Tsirlin, A. A.; Niermann, D.; Waschkowski, F.; Hemberger, J.; Van Tendeloo, G.; Antipov, E. V. *Chem. Mater.* **2011**, *23*, 255–265.

(19) Andersson, S.; Wadsley, A. D. *Nature* **1966**, *211*, 581–583.

(20) Anderson, J. S.; Hyde, B. G. *Bull. Soc. Chim. Fr.* **1965**, 1215–1216.

(21) Van Landuyt, J.; Amelinckx, S. *J. Solid State Chem.* **1973**, *6*, 222–229.

(22) Bursill, L. A.; Hyde, B. G. *J. Solid State Chem.* **1972**, *4*, 430–446.

(23) Hardy, A.; Gielis, S.; Van den Rul, H.; D'Haen, J.; Van Bael, M. K.; Mullens, J. *J. Eur. Ceram. Soc.* **2009**, *29*, 3007–3013.

(24) De Dobbelaere, C.; Hardy, A.; D'Haen, J.; Van den Rul, H.; Van Bael, M. K.; Mullens, J. *J. Eur. Ceram. Soc.* **2009**, *29*, 1703–1711.

(25) Koch, C. . Ph.D. Thesis, Arizona State University, Phoenix, AZ, 2002.

(26) Findlay, S. D.; Shibata, N.; Sawada, H.; Okunishi, E.; Kondo, Y.; Yamamoto, T.; Ikuhara, Y. *Appl. Phys. Lett.* **2009**, *95*, 191913-1 –191913-3.

(27) Findlay, S. D.; Shibata, N.; Sawada, H.; Okunishi, E.; Kondo, Y.; Ikuhara, Y. *Ultramicroscopy* **2010**, *110*, 903–923.

(28) Wojdyr, M. *J. Appl. Crystallogr.* **2010**, *43*, 1126–1128.

(29) Stephens, P. W. *J. Appl. Crystallogr.* **1999**, *32*, 281–289.

(30) Rivolier, J. L.; Ferriol, M.; Abraham, R.; Cohen-Adad, M.-T. *Eur. J. Solid State Inorg. Chem.* **1993**, *30*, 727–739.